ACS APPLIED MATERIALS & INTERFACES

Research Article

www.acsami.org

# Efficiency Enhancement of Nanotextured Black Silicon Solar Cells Using $Al_2O_3/TiO_2$ Dual-Layer Passivation Stack Prepared by Atomic Layer Deposition

Wei-Cheng Wang,[†] Meng-Chen Tsai,[†] Jason Yang,[‡] Chuck Hsu,[§] and Miin-Jang Chen*,[†]

[†]Department of Materials Science and Engineering, National Taiwan University, Taipei 106, Taiwan

[‡]Sino-American Silicon Products Inc., Yilan Branch, Yilan County 26841, Taiwan

[§]Sino-American Silicon Products Inc., Hsinchu Science Park 30075, Taiwan

**ABSTRACT:** In this study, efficient nanotextured black silicon (NBSi) solar cells composed of silicon nanowire arrays and an $Al_2O_3/TiO_2$ dual-layer passivation stack on the $n^+$ emitter were fabricated. The highly conformal $Al_2O_3$ and $TiO_2$ surface passivation layers were deposited on the high-aspect-ratio surface of the NBSi wafers using atomic layer deposition. Instead of the single $Al_2O_3$ passivation layer with a negative oxide charge density, the $Al_2O_3/TiO_2$ dual-layer passivation stack treated with forming gas annealing provides a high positive oxide charge density and a low interfacial state density, which are essential for the effective field-effect and chemical passivation of the $n^+$ emitter. In addition, the $Al_2O_3/TiO_2$ dual-layer passivation stack suppresses the total reflectance over a broad range of wavelengths (400−1000 nm). Therefore, with the $Al_2O_3/TiO_2$ dual-layer passivation stack, the short-circuit current density and efficiency of the NBSi solar cell were increased by 11% and 20%, respectively. In conclusion, a high efficiency of 18.5% was achieved with the NBSi solar cells by using the $n^+$-emitter/p-base structure passivated with the $Al_2O_3/TiO_2$ stack.

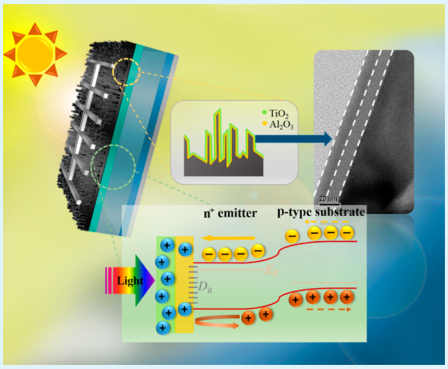


**KEYWORDS:** *nanotextured black silicon, solar cell, silicon nanowire, atomic layer deposition, surface passivation, aluminum oxide ($Al_2O_3$), titanium dioxide ($TiO_2$)*

## INTRODUCTION

In recent years, nanostructured silicon (Si) surfaces have attracted much attention because of their low reflectance over a wide range of wavelengths,[1−6] which causes them to appear black, and therefore they are called "black silicon". These nanotextured black silicon (NBSi) wafers also have good antireflection (AR) properties over a broad range of incident angles.[7−13] These AR characteristics are mainly attributed to the omnidirectional scattering of light, which is caused by the subwavelength structures and refractive index gradient from the substrate to air.[7−13] Therefore, NBSi has been rapidly applied to a variety of solar cells,[12,14−16] including thin-film cells,[17−19] photoelectrochemical cells,[20,21] diffused pn junction cells,[22−24] and solid-state hybrid heterojunction cells.[25] Many NBSi fabrication processes have been developed,[26] such as stain etching,[27] electrochemical etching,[28] reactive-ion etching,[29,30] laser treatments,[31,32] metal-assisted wet chemical etching,[3,6,22,33−36] and the Fray−Farthing−Chen Cambridge process,[37,38] all of which have been comprehensively and clearly reviewed by Liu et al.[26] Of these methods, metal-assisted wet chemical etching benefits from a simple hardware requirement as well as being a cost-effective, fast, and applicable process for the fabrication of such nanostructures. In addition, this technique can be implemented not only on crystalline, multicrystalline, and amorphous Si[36,39] but also on other materials.[40] Hence, silver-catalyzed wet chemical etching was used to fabricate NBSi in this study.

Although NBSi offers superior optical performance, the efficiency of NBSi solar cells is not as high as that of conventional Si solar cells.[41−43] The difficulties in achieving efficient NBSi solar cells are mainly attributed to the enlarged surface area and associated surface defects created by the NBSi fabrication process. The resulting surface recombination deteriorates the efficiency of NBSi solar cells, and therefore suppression of the surface recombination is a critical factor.[26,41−44] Applying a dielectric passivation coating is the conventional method for reducing the surface recombination rate, which works via two mechanisms: (1) chemical passivation, caused by a decrease of the interfacial state density ($D_{it}$); (2) field-effect passivation, in which the built-in electric field reduces the minority-carrier concentration near the interface. This built-in electric field can be established by an equivalent oxide charge density ($Q_{ox}$) with the appropriate polarity in the passivation layer, which then suppresses the surface recombination rate by repelling the minority carriers away from the surface.[44,45] Various dielectric passivation layers

Received: January 22, 2015
Accepted: April 28, 2015
Published: April 28, 2015

  

DOI: 10.1021/acsami.5b00677
ACS Appl. Mater. Interfaces 2015, 7, 10228−10237

have been extensively studied, including silicon oxide ($SiO_2$),[41,46] $SiN_x$,[47,48] and aluminum oxide ($Al_2O_3$).[42,49] Oh et al.[41] used thermally grown $SiO_2$ to passivate NBSi solar cells and achieved a high efficiency of 18.2%. Yue et al.[48] reported large-area NBSi solar cells with efficiencies of over 18% that used $SiN_x$ passivation layers prepared by plasma-enhanced chemical vapor deposition. A high efficiency of 18.45% was achieved by Ye et al.[50] in pseudopyramid-nanotextured, multicrystalline Si solar cells with $SiN_x$ as both the passivation and AR layers. Recently, the $Al_2O_3$ surface passivation layers deposited by atomic layer deposition (ALD) upon the surface of the NBSi have attracted much interest because of the excellent conformality and step coverage of the thin films prepared by ALD.[4,26,49,51,52] Other benefits of ALD include facile and precise thickness control, high uniformity over a wide area, low defect density, and low deposition temperatures, which are the result of the self-limiting layer-by-layer deposition of this technique. In addition, in our previous study,[53] we demonstrated that the chemical inertness, high step coverage, and pinhole-free structure of the conformal $Al_2O_3$ layer provide effective anticorrosion protection for the nanostructures against harmful environments. It has been reported that ALD-$Al_2O_3$ surface passivation layers work well on the front surface of the $p^+$-emitter/n-base and on the rear surface of the $n^+$-emitter/p-base of Si solar cells.[25,26] Repo et al.[42] reported the highly efficient (18.7%) $p^+$-emitter/n-base NBSi solar cells passivated with an ALD-$Al_2O_3$ layer, which had significantly improved surface passivation and light absorption properties. However, ALD-$Al_2O_3$ is inappropriate as the surface passivation layer on the front surface of the $n^+$-emitter/p-base structure because of its negative $Q_{ox}$, which is unfavorable for field-effect passivation.[26,45] However, because the $n^+$-emitter/p-base structure is the most popular solar-cell structure currently used, a surface passivation layer with low $D_{it}$, positive $Q_{ox}$, and high conformality is highly desired for NBSi solar cells with the $n^+$-emitter/p-base structure.

In this study, ALD was used to prepare $Al_2O_3$/titanium dioxide ($TiO_2$) dual-layer passivation stacks on the $n^+$ emitter of efficient NBSi solar cells. The multiple-pulse fabrication scheme was used to deposit highly conformal passivation layers upon the NBSi surface. A $TiO_2$ layer with highly positive $Q_{ox}$ was deposited on the negatively charged $Al_2O_3$ passivation layer, resulting in positive $Q_{ox}$ in the $Al_2O_3/TiO_2$ dual-layer passivation stack. Low $D_{it}$ was achieved by performing forming gas annealing (FGA) on the $Al_2O_3$/Si interface. In addition, the total reflectance of NBSi was further reduced by the $Al_2O_3/TiO_2$ dual-layer passivation stack. Accordingly, an efficiency of up to 18.5% was achieved with the NBSi solar cells that had the $Al_2O_3/TiO_2$ dual-layer passivation stack because of its low $D_{it}$, positive $Q_{ox}$, and high conformality.

## EXPERIMENTAL SECTION

NBSi was fabricated on p-type Si(100) wafers (Czochralski-grown, 0.5−3 Ω·cm, thickness ≈180 μm) with the silver-catalyzed wet chemical etching method. To fabricate the nanostructures, the Si wafers were immersed in a 0.1 M solution of $AgNO_3$ ($AgNO_3$:HF:$H_2O_2$:deionized water = 0.2:4:1.6:8) at room temperature.[54] The wafers were then rinsed with a silver (Ag)-etchant solution ($NH_3OH$:$H_2O_2$ = 3:1) to remove the Ag clusters.[54] A schematic of the structure of the NBSi solar cell is shown in Figure 1. The $n^+$ emitter was doped with phosphorus oxychloride ($POCl_3$) at 825 °C. The diffused junction depth was approximately 0.4 μm, and the surface dopant concentration was approximately $5 \times 10^{20}$ $cm^{-3}$. After the diffusion process, the phosphosilicate glass layer was etched

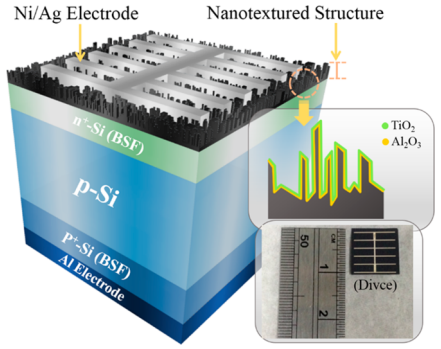


**Figure 1.** Schematic diagram of the NBSi solar cell with the $n^+$-emitter/p-base structure, along with a photograph of the device.

away with a diluted HF solution. The back contact was then screen-printed and fired at 850 °C to form the back surface field. The front nickel/Ag contact was subsequently deposited by thermal evaporation through a shadow mask. The $Al_2O_3$ and $TiO_2$ layers (each of which was approximately 10 nm thick) were then deposited at 200 °C with the ALD system (Fiji, Ultratech). Trimethylaluminum [TMA, $Al(CH_3)_3$] and $H_2O$ vapor were used as the precursors of Al and O for the $Al_2O_3$ deposition process, and tetrakis(dimethylamino)titanium [TDMAT, $Ti(N(CH_3)_2)_4$] and remote $O_2$ plasma were the precursors of Ti and O for the $TiO_2$ deposition process. The precursors were delivered into the reaction chamber by an argon carrier gas. The deposition rates of $Al_2O_3$ and $TiO_2$ were approximately 0.1 and 0.05 nm per ALD cycle, respectively. Because of the high-aspect-ratio surface of NBSi, a multiple-pulse ALD scheme was applied to improve the penetration depth of the precursors in the deep NBSi structures. For example, one ALD cycle for $Al_2O_3$ deposition consisted of four pulses of TMA followed by four pulses of $H_2O$, as shown schematically in Figure 2. During the ALD process, the first TMA pulse yields a

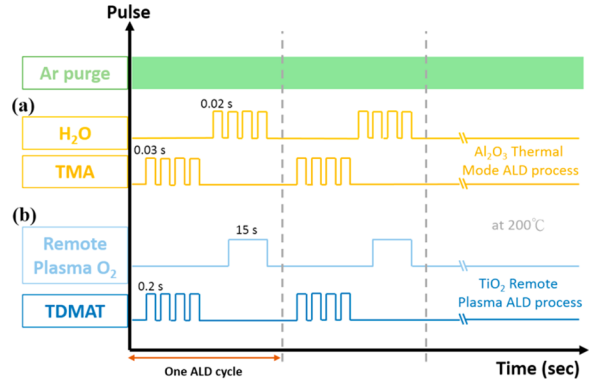


**Figure 2.** Schematic diagram of the multiple-pulse scheme used in the (a) $Al_2O_3$ and (b) $TiO_2$ ALD processes.

methyl-terminated NBSi surface to a depth determined by the amount of precursor deposited. The following TMA pulse is unable to react with the methyl-terminated surface near the top of nanostructures and is only chemisorbed onto the deeper surfaces of NBSi. Thus, by utilization of the multiple-pulse scheme, the precursors can penetrate far into the NBSi layer. The multiple $H_2O$ pulses then react with TMA chemisorbed on the surface of NBSi to finish one complete ALD cycle for $Al_2O_3$.[52,55] Finally, FGA ($H_2$:$N_2$ = 5:95) treatment was performed at 400 °C to reduce $D_{it}$ and, hence, improve the efficiency.

Scanning electron microscopy (SEM; Nova NanoSEM 450) and high-resolution transmission electron microscopy with energy-dispersive X-ray spectroscopy (HR-TEM with EDS; JEM-2100F electron microscope, JEOL Co., 200 kV) were used to characterize the morphology of NBSi. The total reflectance spectra of the NBSi wafers were measured with a spectrophotometer equipped with integrating


DOI: 10.1021/acsami.5b00677
ACS Appl. Mater. Interfaces 2015, 7, 10228−10237

spheres (AVANTES Avalight-HAL-S and AvaSpec-2048L). To determine the $D_{it}$ and $Q_{ox}$ values of the surface passivation layers, all samples were electrically probed with an Agilent B1500A semiconductor device analyzer to measure the high-frequency (100 kHz) capacitance−voltage ($C-V$) curves of the metal-oxide-semiconductor (MOS) capacitors at room temperature in an electrically shielded, light-proof probe station. Platinum (Pt) and polished p-type Si(100) wafers with resistivities of 1−10 Ω·cm were used as the gate metal and substrate of the MOS capacitors, respectively. The effective minority-carrier lifetime of the samples was measured with the quasi-steady-state photoconductance (QSSPC) technique (Sinton WCT-120 lifetime tester). The efficiency of the NBSi solar cells was examined with an active area of 0.92 $cm^2$ exposed to AM 1.5 (100 mW $cm^{-2}$ at 25 °C) illumination from a solar simulator, which was calibrated with a standard Si solar cell before the measurements. The external quantum efficiency (EQE) measurements were performed with a QEX7 solar-cell spectral response measurement system at room temperature.

## RESULTS AND DISCUSSION

Top-view and cross-sectional SEM images of NBSi are shown in parts a and b of Figure 3, respectively, and they reveal the densely packed, vertically aligned Si nanowires. The height of the nanowires is between 0.5 and 1 $\mu$m, and their diameter ranges from 50 to 150 nm. Therefore, the spatial separation and dimensions of the Si nanowires are smaller than the wavelengths that comprise sunlight. The subwavelength structures can effectively suppress the reflectance because of the strong optical scattering and thus enhance the optical absorption of the NBSi wafers.[7−13]

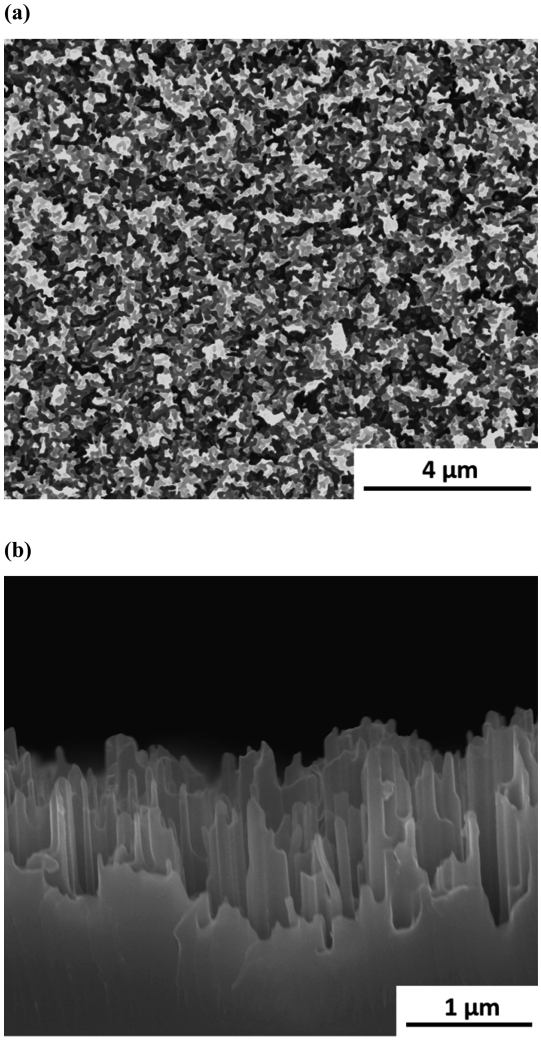


**Figure 3.** (a) Top-view and (b) cross-sectional SEM images of the surface morphology of NBSi.

Figure 4a shows the total reflectance of the polished Si, textured Si, and NBSi for wavelengths ranging from 400 to 1000 nm. Compared to the polished and textured Si wafers, the NBSi wafer exhibits a much lower total reflectance over the entire spectral range tested. The total reflectance of the NBSi wafer is approximately 3.5% in the broad-wavelength region from 400 to 800 nm and slightly increases for wavelengths greater than 800 nm. This low reflectance is caused by the nanotextured morphology of the NBSi surface. The subwavelength nanostructures create a refractive index gradient from the top to the bottom of the Si nanowires,[10−13] which means the Si nanowire arrays can act like a multilayer AR coating with the ability to suppress the total reflectance over a wide range of wavelengths. Figure 4b shows the total reflectance for the NBSi samples covered with $Al_2O_3$, $TiO_2$, and the $Al_2O_3/TiO_2$ dual-layer passivation stack. Compared to the pristine NBSi wafer, it can be seen that the total reflectance is reduced by the individual $Al_2O_3$ and $TiO_2$ passivation layers. The $Al_2O_3/TiO_2$ dual-layer passivation stack causes a further

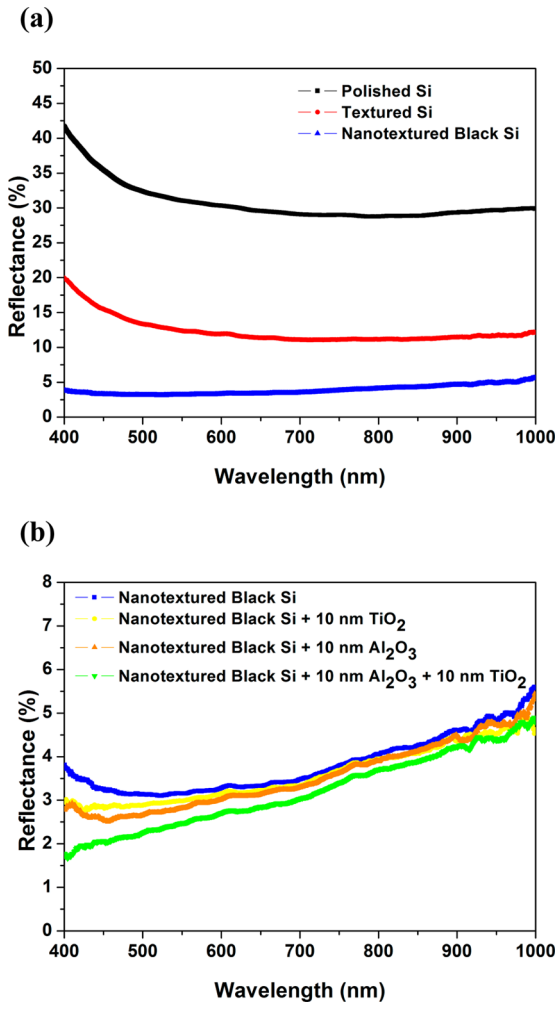


**Figure 4.** Total reflectance spectra of (a) polished Si, textured Si, and NBSi and (b) NBSi covered with the $Al_2O_3$, $TiO_2$, and $Al_2O_3/TiO_2$ passivation layers.


DOI: 10.1021/acsami.5b00677
ACS Appl. Mater. Interfaces 2015, 7, 10228−10237

decrease in the total reflectance, with the reflectance ranging from 1.5 to 2.5% between 400 and 700 nm. This enhanced reduction in the total reflectance could be attributed to the refractive index gradient caused by the insertion of a low refractive index layer between NBSi and air.

Parts a and b of Figure 5 show low- and high-magnification HR-TEM images of the Si nanowires covered with the $Al_2O_3$/$TiO_2$ dual-layer passivation stack. The HR-TEM images clearly show that the Si nanowires are encased in the dual $Al_2O_3$/$TiO_2$ layers, demonstrating the high conformality and excellent step coverage of the multiple-pulse ALD scheme. The thickness of each $Al_2O_3$ and $TiO_2$ layer is approximately 10 nm, which is consistent with the thicknesses estimated for the 100 and 200 cycles of the $Al_2O_3$ and $TiO_2$ ALD processes, respectively. The EDS mapping results shown in Figure 6, along with an image of the scanned region, reveal the elemental distributions of the Si nanowire coated with the dual $Al_2O_3$/$TiO_2$ layers. The distribution profiles of O, Si, Al, and Ti further confirm that the Si nanowires are surrounded by the $Al_2O_3$/$TiO_2$ dual-layer passivation stack.

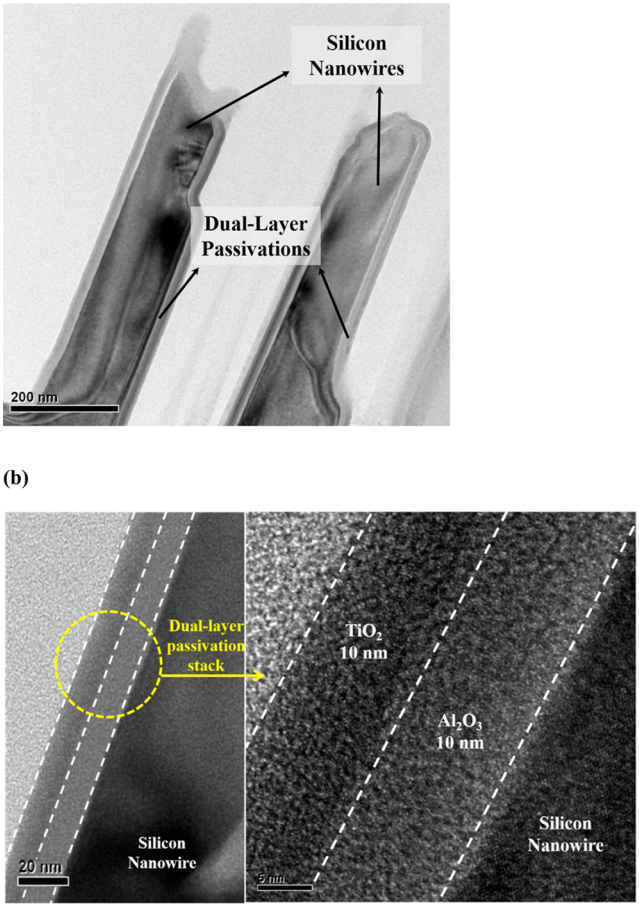


**Figure 5.** (a) Low- and (b) high-magnification TEM images of the Si nanowires encased in the $Al_2O_3$/$TiO_2$ dual-layer passivation stack.

Figure 7 shows the normalized $C-V$ curves of the Si/$Al_2O_3$/Pt, Si/$TiO_2$/Pt, and Si/($Al_2O_3$/$TiO_2$ stack)/Pt MOS capacitors, where the capacitance was normalized to the maximum capacitance of each sample. It should be noted that the terms "FGA-treated" and "as-deposited" represent the dielectric layer

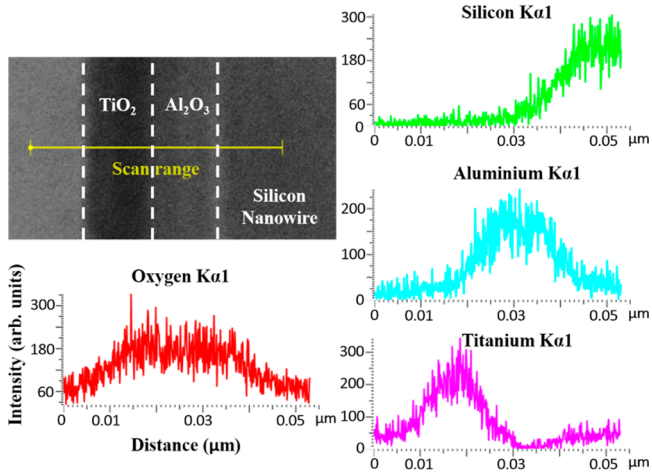


**Figure 6.** EDS mapping results showing the elemental distributions of the Si nanowires encased in the $Al_2O_3$/$TiO_2$ dual-layer passivation stack. The red, green, blue, and purple lines represent the distributions of O, Si, Al, and Ti, respectively.

with and without the FGA treatment, respectively. For the capacitors with the $Al_2O_3$/$TiO_2$ dual-layer stack, the FGA treatment was carried out before or after the $TiO_2$ deposition, which are denoted as the $Al_2O_3$/FGA/$TiO_2$ and $Al_2O_3$/$TiO_2$/FGA samples in Figure 7 and Table 1, respectively. The flat-band voltage $V_{fb}$ was extracted from the flat-band capacitance $C_{fb}$ in the $C-V$ curves, and $Q_{ox}$ was calculated from the shift in $V_{fb}$ with respect to the ideal $V_{fb}$, which can be determined from the differences between the work functions of Pt (5.22 eV for Pt on $Al_2O_3$[56] and 5.5 eV for Pt on $TiO_2$[57,58]) and Si (4.875 eV). $D_{it}$ at the midgap was calculated from the $C-V$ curves with the Terman method.[59] Figure 7b shows an obvious shoulder in the $C-V$ curve of the as-deposited $TiO_2$ sample, which indicates that many interfacial states exist at the $TiO_2$/Si interface. Hence, as shown in Table 1, $D_{it}$ of the as-deposited $TiO_2$ capacitor is much higher than that of the as-deposited $Al_2O_3$ capacitor. After the FGA treatment, $D_{it}$ has been reduced by 1 order of magnitude not only in the $Al_2O_3$ and $TiO_2$ capacitors but also in the capacitors with the $Al_2O_3$/$TiO_2$ dual-layer stack (the $Al_2O_3$/FGA/$TiO_2$ and $Al_2O_3$/$TiO_2$/FGA samples). This is further evidenced by the shoulder nearly vanishing in the $C-V$ curve of the FGA-treated $TiO_2$ capacitor. The reduction in $D_{it}$ can be ascribed to the interfacial states being passivated by $H_2$ in the forming gas.[59,60] It should be noted that, as shown in Figure 7b, the capacitance of both the as-deposited and FGA-treated $TiO_2$ capacitors sharply decreases in the accumulation region (negative gate voltages greater than approximately −1.5 V). This can be attributed to the high leakage current due to the low band gap (3.5 eV) of $TiO_2$.[61]

Although the FGA treatment improves chemical passivation (decreases $D_{it}$), it hinders field-effect passivation. Figure 7a shows that the FGA treatment causes the normalized $C-V$ curve of the Si/$Al_2O_3$/Pt capacitor to shift considerably in the positive voltage direction, indicating that the polarity of $Q_{ox}$ has changed from positive to negative (Table 1). This result is in good agreement with the literature.[52,62,63] The detailed investigations and discussions of the negative $Q_{ox}$ of ALD-$Al_2O_3$ can be found in the literature.[64−66] This negative $Q_{ox}$ is detrimental to field-effect passivation on the front surface of the $n^+$-emitter/p-base solar cell structure. Unlike $Al_2O_3$, Table 1


DOI: 10.1021/acsami.5b00677
ACS Appl. Mater. Interfaces 2015, 7, 10228−10237

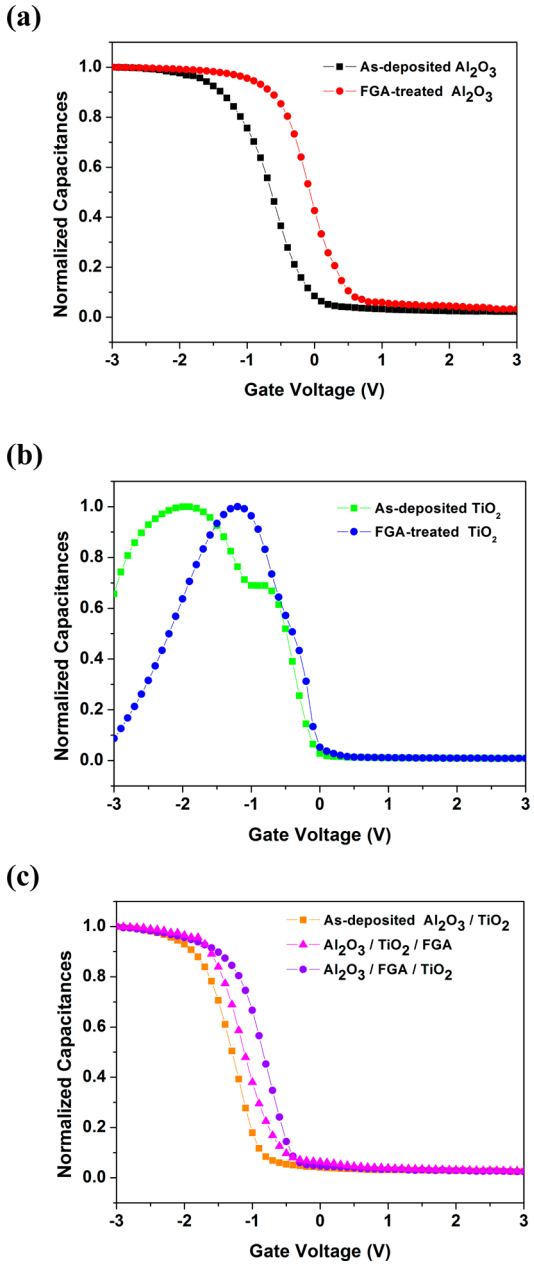


**Figure 7.** Normalized $C-V$ curves of the (a) as-deposited and FGA-treated $Al_2O_3$ MOS capacitors, (b) as-deposited and FGA-treated $TiO_2$ MOS capacitors, and (c) as-deposited $Al_2O_3/TiO_2$, $Al_2O_3$/FGA/$TiO_2$, and $Al_2O_3/TiO_2$/FGA MOS capacitors. Pt and polished p-type Si(100) wafers were used as the gate metal and substrate of the MOS capacitors, respectively.

shows that $Q_{ox}$ of as-deposited and FGA-treated $TiO_2$ is positive, which is consistent with the results reported by others.[67,68] However, $D_{it}$ of FGA-treated $TiO_2$ is much higher than that of FGA-treated $Al_2O_3$. Therefore, a stacked structure was proposed for this study, with $TiO_2$ deposited on the $Al_2O_3$ layer and subjected to FGA, to achieve a surface passivation with a positive $Q_{ox}$ and low $D_{it}$, which are provided by the $TiO_2$ and $Al_2O_3$ layers, respectively. Figure 7c and Table 1 show that the as-deposited $Al_2O_3/TiO_2$ stack exhibits a highly positive $Q_{ox}$ of $5.48 \times 10^{12}$ $cm^{-2}$. Again, the FGA treatment results in the normalized $C-V$ curves of the $Al_2O_3$/FGA/$TiO_2$ and $Al_2O_3/TiO_2$/FGA samples to shift in the positive voltage direction, indicating a decrease in the overall positive $Q_{ox}$ value of the

**Table 1. Equivalent Oxide Charge Density ($Q_{ox}$) and Interfacial State Density ($D_{it}$) of the $Al_2O_3$, $TiO_2$, and $Al_2O_3/TiO_2$ Passivation Layers, Which Were Extracted from the $C-V$ Curves Shown in Figure 7**

| | $Q_{ox}/q$ ($cm^{-2}$) | $D_{it}$ ($cm^{-2}$ $eV^{-1}$) |
|---|---|---|
| as-deposited $Al_2O_3$ (cell 2) | $1.27 \times 10^{12}$ | $3.94 \times 10^{12}$ |
| $Al_2O_3$/FGA (cell 3) | $-3.10 \times 10^{11}$ | $2.61 \times 10^{11}$ |
| as-deposited $TiO_2$ (cell 4) | $7.36 \times 10^{12}$ | $1.15 \times 10^{13}$ |
| $TiO_2$/FGA (cell 5) | $6.28 \times 10^{12}$ | $1.79 \times 10^{12}$ |
| as-deposited $Al_2O_3/TiO_2$ (cell 6) | $5.48 \times 10^{12}$ | $7.59 \times 10^{12}$ |
| $Al_2O_3$/FGA/$TiO_2$ (cell 7) | $4.10 \times 10^{12}$ | $5.33 \times 10^{11}$ |
| $Al_2O_3/TiO_2$/FGA (Cell 8) | $4.66 \times 10^{12}$ | $3.91 \times 10^{11}$ |

$Al_2O_3/TiO_2$ stacks (Table 1). This decrease in the overall positive $Q_{ox}$ value, which is caused by the FGA treatment, can be understood by the presence of a negative $Q_{ox}$ in the $Al_2O_3$ layer.

The evolution of $Q_{ox}$ and $D_{it}$ in the various $Al_2O_3/TiO_2$ stacks is displayed in Figure 8. As shown in Figure 8a, the FGA

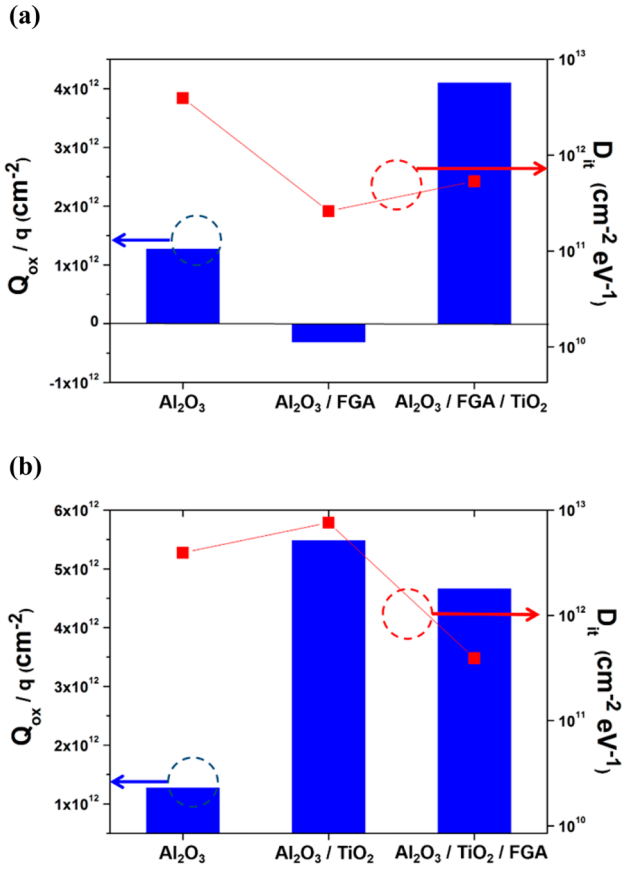


**Figure 8.** Evolution of $Q_{ox}$ and $D_{it}$ with different surface passivation layers: (a) $Al_2O_3$, $Al_2O_3$/FGA, and $Al_2O_3$/FGA/$TiO_2$ (b) $Al_2O_3$, $Al_2O_3/TiO_2$, and $Al_2O_3/TiO_2$/FGA. The values were determined from the $C-V$ curves shown in Figure 7.

treatment of the as-deposited $Al_2O_3$ layer results in a negative $Q_{ox}$ and a significant decrease in $D_{it}$. Depositing $TiO_2$ on FGA-treated $Al_2O_3$ changes $Q_{ox}$ from negative to positive. As for the $Al_2O_3/TiO_2$/FGA sample shown in Figure 8b, deposition of $TiO_2$ on the as-deposited $Al_2O_3$ gives rise to an increase of positive $Q_{ox}$, and the subsequent FGA treatment causes a considerable decrease in $D_{it}$. Table 1 shows that the $Al_2O_3$/


DOI: 10.1021/acsami.5b00677
ACS Appl. Mater. Interfaces 2015, 7, 10228−10237

Table 2. $V_{oc}$, $J_{sc}$, FF, and $\eta$ of the NBSi Solar Cells with Different Surface Passivation Layers

| | $V_{oc}$ (mV) | $J_{sc}$ (mA cm$^{-2}$) | FF (%) | $\eta$ (%) |
|---|---|---|---|---|
| cell 1 (without passivation) | 572 ± 4.3 | 35.37 ± 0.14 | 76.47 ± 0.03 | 15.4 ± 0.06 |
| cell 2 (as-deposited $Al_2O_3$) | 580 ± 0.002 | 36.84 ± 0.26 | 77.80 ± 0.45 | 16.6 ± 0.02 |
| cell 3 ($Al_2O_3$/FGA) | 595 ± 5.02 | 38.3 ± 0.62 | 78.91 ± 0.89 | 18.1 ± 0.03 |
| cell 4 (as-deposited $TiO_2$) | 580 ± 0.001 | 35.71 ± 0.21 | 76.34 ± 0.33 | 15.8 ± 0.16 |
| cell 5 ($TiO_2$/FGA) | 585 ± 5.0 | 37.32 ± 0.07 | 78.01 ± 0.43 | 17.1 ± 0.03 |
| cell 6 (as-deposited $Al_2O_3$/$TiO_2$) | 590 ± 0.001 | 37.13 ± 0.31 | 76.57 ± 0.52 | 16.7 ± 0.03 |
| cell 7 ($Al_2O_3$/FGA/$TiO_2$) | 590 ± 0.01 | 40.38 ± 0.10 | 76.84 ± 0.08 | 18.3 ± 0.03 |
| cell 8 ($Al_2O_3$/$TiO_2$/FGA) | 590 ± 0.002 | 39.26 ± 0.20 | 79.87 ± 0.32 | 18.5 ± 0.02 |
| cell R1 (as-deposited $TiO_2$/$Al_2O_3$) | 593 ± 4.73 | 34.97 ± 0.66 | 76.2 ± 0.85 | 16.0 ± 0.18 |
| cell R2 ($TiO_2$/$Al_2O_3$/FGA) | 590 ± 0.003 | 38.94 ± 0.02 | 75.88 ± 0.11 | 17.4 ± 0.02 |

Table 3. $V_{oc}$, $J_{sc}$, FF, and $\eta$ of Conventionally Textured Si Solar Cells Passivated with the As-Deposited and FGA-Treated $TiO_2$/$Al_2O_3$ Dual-Layer Stacks, Where Cell T1 Is the Textured Si Solar Cell without Any Passivation Layer

| | $V_{oc}$ (mV) | $J_{sc}$ (mA cm$^{-2}$) | FF (%) | $\eta$ (%) |
|---|---|---|---|---|
| cell T1 (without passivation) | 593 ± 0.005 | 36.19 ± 0.05 | 74.17 ± 0.42 | 15.9 ± 0.05 |
| cell T2 (as-deposited $Al_2O_3$/$TiO_2$) | 603 ± 0.007 | 39.39 ± 0.63 | 74.56 ± 0.71 | 17.7 ± 0.15 |
| cell T3 ($Al_2O_3$/$TiO_2$/FGA) | 597 ± 0.01 | 39.53 ± 0.12 | 75.76 ± 0.04 | 17.9 ± 0.03 |

$TiO_2$ dual-layer stack combined with the FGA treatment achieves a highly positive $Q_{ox}$ (on the order of $10^{12}$ cm$^{-2}$) and low $D_{it}$ (on the order of $10^{11}$ cm$^{-2}$ eV$^{-1}$) for both the $Al_2O_3$/FGA/$TiO_2$ and $Al_2O_3$/$TiO_2$/FGA samples.

Table 2 shows the open-circuit voltage ($V_{oc}$), short-circuit current density ($J_{sc}$), fill-factor (FF), and efficiency ($\eta$) of the NBSi solar cells, where cell 1 represents the NBSi solar cell without any passivation layer. The surface passivation layers in cells 2−8 correspond to those shown in Table 1. From Tables 1 and 2, it can be seen that high $D_{it}$ of the as-deposited $Al_2O_3$, as-deposited $TiO_2$, $TiO_2$/FGA, and as-deposited $Al_2O_3$/$TiO_2$ surface passivation layers (cells 2, 4, 5, and 6, respectively) results in solar cells with low values of $\eta$. However, the surface passivation layers with low $D_{it}$ (on the order of $10^{11}$ cm$^{-2}$ eV$^{-1}$), such as the $Al_2O_3$/FGA, $Al_2O_3$/FGA/$TiO_2$, and $Al_2O_3$/$TiO_2$/FGA layers, result in solar cells with high values of $\eta$ (greater than 18% in cells 3, 7, and 8, respectively). On the other hand, even though the positive and large values of $Q_{ox}$ in cells 4, 5, and 6 enhance field-effect passivation, the efficiency of these solar cells is still low because of their high $D_{it}$ values. These results clearly indicate that low $D_{it}$ is essential for a high efficiency. It should be noted that the efficiency of cell 7 (positive and large $Q_{ox}$) is greater than that of cell 3 (negative $Q_{ox}$), even though $D_{it}$ of cell 3 is lower than that of cell 7. This clearly demonstrates the effect of field-effect passivation caused by $Q_{ox}$ with appropriate polarity. Compared to cell 7, the increased positive $Q_{ox}$ and decreased $D_{it}$ values of cell 8 result in a further enhancement of $\eta$.

In addition, we have fabricated the NBSi solar cells passivated with as-deposited and FGA-treated $TiO_2$/$Al_2O_3$ dual-layer stacks, and their performance is also shown in Table 2. It could be clearly seen that the efficiency of cell R1 (as-deposited $TiO_2$/$Al_2O_3$) is lower than that of cell 6 (as-deposited $Al_2O_3$/$TiO_2$), and the performance of cell R2 ($TiO_2$/$Al_2O_3$/FGA) is also inferior to that of cell 8 ($Al_2O_3$/$TiO_2$/FGA). Because $D_{it}$ of as-deposited and FGA-treated $TiO_2$ is approximately 1 order of magnitude greater than that of as-deposited and FGA-treated $Al_2O_3$, as shown in Table 1, the efficiency of the NBSi solar cells passivated with $TiO_2$/$Al_2O_3$ is not superior to those with the $Al_2O_3$/$TiO_2$ dual-layer passivation stack. The result indicates that the interface quality between the surface passivation layer and Si is a key point in the selection of materials for the passivation layers.

Table 2 also show that the $V_{oc}$ values of the NBSi solar cells are lower than those of commercial Si-based solar cells, which can be attributed to three mechanisms: (1) the enlarged surface area of NBSi increases the number of surface recombination centers; (2) the nonuniform and heavy doping concentration in the emitter, which is due to the high-aspect-ratio surface of NBSi, results in severe Auger recombination; (3) localized shunting paths are formed because of the poor metal contact with the NBSi surface.[22,26]

On the other hand, we also used the standard surface texturing and the same pn junction diffusion processes to fabricate conventionally textured Si solar cells, which were passivated with the as-deposited and FGA-treated $Al_2O_3$/$TiO_2$ dual-layer stacks. Their performance is presented in Table 3. A comparison of cells T1 and T3 shows that $J_{sc}$ and $\eta$ increase by 9.2% and 12.6%, respectively, and $V_{oc}$ is also slightly increased by the $Al_2O_3$/$TiO_2$/FGA dual-layer passivation stack. However, compared with cell T2, the FGA treatment does not induce a significant increase in the efficiency of cell T3. This may be because the amount of surface recombination centers of textured Si is not as much as that of NBSi. Thus, the effect of the FGA treatment on the textured Si is not obvious compared with that on the NBSi solar cells. In addition, one can find that cell T1 (textured Si without passivation) exhibited a relatively higher efficiency than cell 1 (NBSi without passivation), which may be caused by a large amount of surface defects even though NBSi exhibited significantly low reflectance. However, after surface passivation by the $Al_2O_3$/$TiO_2$ dual-layer stack and FGA treatment, the efficiency of cell 8 (NBSi with $Al_2O_3$/$TiO_2$/FGA) is higher than that of cell T3 (textured Si with $Al_2O_3$/$TiO_2$/FGA). The result indicates that surface recombination of NBSi is effectively suppressed by the $Al_2O_3$/$TiO_2$/FGA dual-layer passivation stack, and so we can see the benefit of low reflectance of NBSi. Hence, the advantage of NBSi is mainly low reflectance over a broad range of wavelengths and incident angles. However, the efficiency of NBSi solar cells is limited by significant carrier recombination caused by the enlarged and damaged surface. Thus, suppression of the surface recombination is critical to NBSi solar cells.


DOI: 10.1021/acsami.5b00677
ACS Appl. Mater. Interfaces 2015, 7, 10228−10237

Because of the high-aspect-ratio surface of NBSi, it is appropriate to use the ALD technique for preparing a surface passivation layer with high conformality and step coverage on the Si nanowires.

The illuminated current−voltage ($I$−$V$) curves of cells 1, 2, 3, and 7 are shown in Figure 9a. Comparing cells 1 and 2 shows

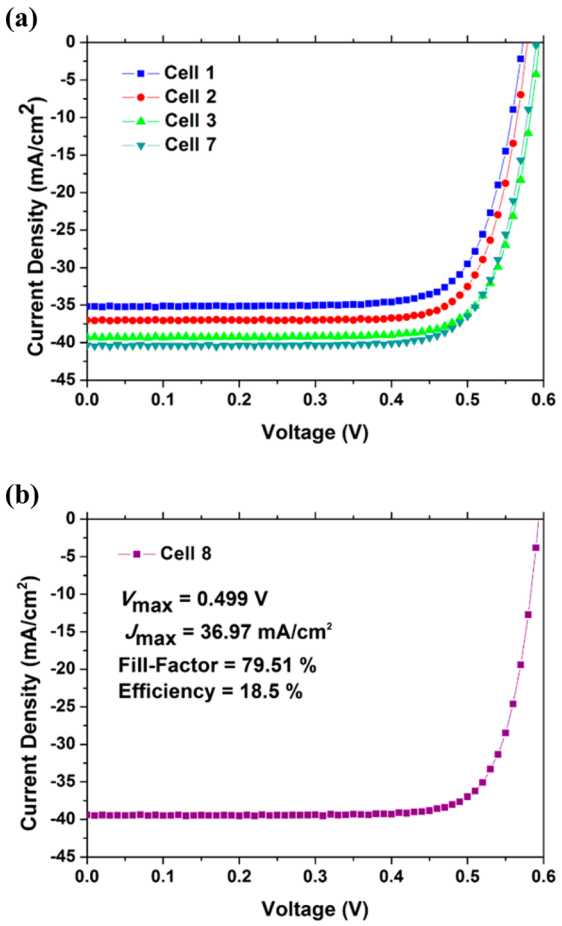


**Figure 9.** Illuminated $I$−$V$ characteristics of (a) cells 1, 2, 3, and 7 and (b) cell 8.

that $J_{sc}$ and $\eta$ increase by 4.2% and 7.8%, respectively, and $V_{oc}$ is also slightly increased by the as-deposited $Al_2O_3$ layer. The enhanced efficiency can be attributed to the increased $J_{sc}$, which is caused by the decreased surface recombination rate, and the increased light absorption, which is due to the reduced total reflectance by the $Al_2O_3$ passivation layer (Figure 4b). After the FGA treatment, $V_{oc}$, $J_{sc}$, FF, and $\eta$ of cell 3 have increased, which can mostly be ascribed to the significantly decreased $D_{it}$ due to the FGA treatment. The deposition of $TiO_2$ on top of the $Al_2O_3$ layer results in a further increase in $J_{sc}$ and $\eta$ of cell 7, which could be attributed to the presence of positive $Q_{ox}$ (Table 1). Figure 9b shows the illuminated $I$−$V$ curve of cell 8, which has the $Al_2O_3/TiO_2$/FGA surface passivation stack, and it has a high efficiency of 18.5%. Compared to cell 1 (no surface passivation), $J_{sc}$ and $\eta$ of cell 8 have increased by 11% and 20%, respectively, which can be ascribed to the favorable characteristics of a positive $Q_{ox}$ and low $D_{it}$ (Table 1). The experimental errors in terms of "average ± standard deviation" are shown in Tables 2 and 3. It can be seen that the overall trend of experimental data is consistent, demonstrating the good repeatability of the experiments.

The effects of surface passivation were further confirmed by the QSSPC and EQE measurements. The effective minority-carrier lifetimes ($\tau$) and implied one-sun open-circuit voltages (implied-$V_{oc}$) at a minority-carrier density of $1 \times 10^{15}$ $cm^{-3}$ in the NBSi solar cells were determined from the QSSPC measurements, and the results are displayed in Table 4. Note

**Table 4. Effective Minority-Carrier Lifetime ($\tau$) and Implied One-Sun Open-Circuit Voltage (Implied-$V_{oc}$) of the NBSi Solar Cells with Different Surface Passivation Layers**

| | effective minority-carrier lifetime ($\mu$s) | implied one-sun open-circuit voltage (mV) |
|---|---|---|
| cell 1 (without passivation) | 7.32 | 575 |
| cell 2 (as-deposited $Al_2O_3$) | 19.84 | 599 |
| cell 3 ($Al_2O_3$/FGA) | 23.91 | 604 |
| cell 4 (as-deposited $TiO_2$) | 17.02 | 594 |
| cell 5 ($TiO_2$/FGA) | 23.54 | 603 |
| cell 6 (as-deposited $Al_2O_3/TiO_2$) | 23.42 | 603 |
| cell 7 ($Al_2O_3$/FGA/$TiO_2$) | 34.17 | 616 |
| cell 8 ($Al_2O_3/TiO_2$/FGA) | 34.25 | 619 |

that QSSPC measures the average excess carrier concentration with an assumption that the carrier concentration is constant through the base, which gives the so-called "implied-$V_{oc}$". The difference between the device-$V_{oc}$ (as shown in Table 2) and implied-$V_{oc}$ could be mainly ascribed to the carrier recombination around the pn junction, which reduces the carrier concentration and, in turn, lowers the device-$V_{oc}$. However, the QSSPC measurement depends on the average carrier concentration, which is higher than that around the junction, resulting in an overestimated implied-$V_{oc}$. Hence, the higher implied-$V_{oc}$ than the device-$V_{oc}$ is attributed to the carrier recombination around the pn junction of the cells.[69] Even though the values of implied-$V_{oc}$ are different from those of device-$V_{oc}$, the variation trend of the implied-$V_{oc}$ and device-$V_{oc}$ with the surface passivation layer (from cell 1 to 8) is quite consistent.

Figure 10 shows the EQE of cells 1, 2, 3, 7, and 8 as a function of the wavelength (300−1100 nm). It is clear that all

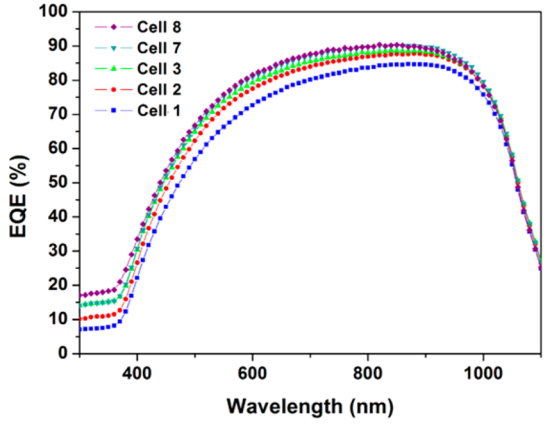


**Figure 10.** EQE of cells 1, 2, 3, 7, and 8 as a function of the wavelength.


DOI: 10.1021/acsami.5b00677
ACS Appl. Mater. Interfaces 2015, 7, 10228−10237

of the cells with surface passivation layers exhibited higher EQEs than cell 1 across the entire spectral range tested. The decreased surface recombination rate and total reflectance of the cells with surface passivation layers, as shown in Table 4 and Figure 4b, are responsible for the increases in EQE. Compared to the NBSi solar cell without a surface passivation layer (cell 1), $\tau$, implied-$V_{oc}$, and EQE are significantly enhanced by the as-deposited $Al_2O_3$ layer (cell 2). After the FGA treatment, decreased $D_{it}$ increases $\tau$, implied-$V_{oc}$, and EQE of cell 3. Further increases in the $\tau$, implied-$V_{oc}$, and EQE occur after the deposition of $TiO_2$ on the FGA-treated $Al_2O_3$ layer (cell 7), which are ascribed to the negative-to-positive conversion of $Q_{ox}$ (Table 1). Compared to cell 7, increased $\tau$, implied-$V_{oc}$, and EQE of cell 8 can be attributed to a further decrease in $D_{it}$ and an increase in positive $Q_{ox}$, as shown in Table 1. The low EQEs at short wavelengths (300−500 nm) are the result of a high Auger recombination rate, which is caused by the formation of a heavily doped "dead layer" in the nanostructured Si because of the high-aspect-ratio nanostructures at the NBSi surface.[41,50] The evolution of $\tau$, implied-$V_{oc}$, and EQE with the various surface passivation layers is very consistent with the $D_{it}$, $Q_{ox}$, and $\eta$ values of the NBSi solar cells that are shown in Tables 1 and 2. Therefore, it can be concluded that the combination of the $Al_2O_3/TiO_2$ dual-layer passivation stack and FGA treatment could provide not only the required chemical passivation (low $D_{it}$) but also an effective field-effect passivation (highly positive $Q_{ox}$), both of which are needed to achieve high-efficiency NBSi solar cells with the $n^+$-emitter/p-base structure.

## CONCLUSIONS

The NBSi wafers were fabricated with silver-catalyzed wet chemical etching, with the resulting subwavelength nanostructures producing omnidirectional and broad-band AR effects. The multiple-pulse ALD scheme was exploited to deposit a highly conformal $Al_2O_3/TiO_2$ dual-layer passivation stack upon the NBSi surface. Low $D_{it}$ and highly positive $Q_{ox}$ of the FGA-treated $Al_2O_3/TiO_2$ dual-layer passivation stack contribute to the effective chemical and field-effect passivation on the $n^+$ emitter, suppressing the surface recombination rate, which was indicated by significant increases in the implied-$V_{oc}$ and $\tau$. In addition, the $Al_2O_3/TiO_2$ dual-layer passivation stack not only reduces the surface recombination rate but also further suppresses the total reflectance over a broad spectral range. $J_{sc}$ and $\eta$ of the solar cell with the FGA-treated $Al_2O_3/TiO_2$ dual-layer passivation stack were increased by 11% and 20%, respectively, compared to the NBSi solar cell without any surface passivation. Hence, a high-efficiency (18.5%) NBSi solar cell was achieved by application of the FGA-treated $Al_2O_3/TiO_2$ dual-layer passivation stack. Therefore, the ALD-fabricated dual-layer passivation stack with high step coverage is a very promising route for achieving efficient NBSi solar cells with the $n^+$-emitter/p-base structure.

## AUTHOR INFORMATION

### Corresponding Author

*E-mail: mjchen@ntu.edu.tw.

### Notes

The authors declare no competing financial interest.

## ACKNOWLEDGMENTS

This work was partially financially supported by National Science Council in Taiwan under contract number NSC 103-2112-M-002 -013 -MY3, 103-2218-E-002 -003, and 103-2120-M-002 -001.

## REFERENCES

(1) Garnett, E.; Yang, P. D. Light Trapping in Silicon Nanowire Solar Cells. *Nano Lett.* **2010**, *10*, 1082−1087.
(2) Han, S. E.; Chen, G. Toward the Lambertian Limit of Light Trapping in Thin Nanostructured Silicon Solar Cells. *Nano Lett.* **2010**, *10*, 4692−4696.
(3) Lu, Y. T.; Barron, A. R. Nanopore-Type Black Silicon Anti-Reflection Layers Fabricated by a One-Step Silver-Assisted Chemical Etching. *Phys. Chem. Chem. Phys.* **2013**, *15*, 9862−9870.
(4) Otto, M.; Kroll, M.; Kasebier, T.; Salzer, R.; Tunnermann, A.; Wehrspohn, R. B. Extremely Low Surface Recombination Velocities in Black Silicon Passivated by Atomic Layer Deposition. *Appl. Phys. Lett.* **2012**, *100*, 191603.
(5) Pei, T. H.; Thiyagu, S.; Pei, Z. Ultra High-Density Silicon Nanowires for Extremely Low Reflection in Visible Regime. *Appl. Phys. Lett.* **2011**, *99*, 153108.
(6) Srivastava, S. K.; Kumar, D.; Singh, P. K.; Kar, M.; Kumar, V.; Husain, M. Excellent Antireflection Properties of Vertical Silicon Nanowire Arrays. *Sol. Energy Mater. Sol. C* **2010**, *94*, 1506−1511.
(7) Chang, H. C.; Lai, K. Y.; Dai, Y. A.; Wang, H. H.; Lin, C. A.; He, J. H. Nanowire Arrays with Controlled Structure Profiles for Maximizing Optical Collection Efficiency. *Energy Environ. Sci.* **2011**, *4*, 2863−2869.
(8) Huang, Y. F.; Chattopadhyay, S.; Jen, Y. J.; Peng, C. Y.; Liu, T. A.; Hsu, Y. K.; Pan, C. L.; Lo, H. C.; Hsu, C. H.; Chang, Y. H.; Lee, C. S.; Chen, K. H.; Chen, L. C. Improved Broadband and Quasi-Omnidirectional Anti-Reflection Properties with Biomimetic Silicon Nanostructures. *Nat. Nanotechnol.* **2007**, *2*, 770−774.
(9) Kanamori, Y.; Sasaki, M.; Hane, K. Broadband Antireflection Gratings Fabricated upon Silicon Substrates. *Opt. Lett.* **1999**, *24*, 1422−1424.
(10) Lin, Y. R.; Lai, K. Y.; Wang, H. P.; He, J. H. Slope-Tunable Si Nanorod Arrays with Enhanced Antireflection and Self-Cleaning Properties. *Nanoscale* **2010**, *2*, 2765−2768.
(11) Pignalos, P.; Lee, H.; Qiao, L.; Tseng, M.; Yi, Y. Graded Index and Randomly Oriented Core-Shell Silicon Nanowires for Broadband and Wide Angle Antireflection. *AIP Adv.* **2011**, *1*, 032124.
(12) Xie, W. Q.; Oh, J. I.; Shen, W. Z. Realization of Effective Light Trapping and Omnidirectional Antireflection in Smooth Surface Silicon Nanowire Arrays. *Nanotechnology* **2011**, *22*, 065704.
(13) Yeo, C. I.; Kim, J. B.; Song, Y. M.; Lee, Y. T. Antireflective Silicon Nanostructures with Hydrophobicity by Metal-Assisted Chemical Etching for Solar Cell Applications. *Nanoscale Res. Lett.* **2013**, *8*, 159.
(14) Steglich, M.; Zilk, M.; Bingel, A.; Patzig, C.; Kasebier, T.; Schrempel, F.; Kley, E. B.; Tunnermann, A. A Normal-Incidence PtSi Photoemissive Detector with Black Silicon Light-Trapping. *J. Appl. Phys.* **2013**, *114*, 183102.
(15) Torres-Costa, V.; Martin-Palma, R. J. Application of Nanostructured Porous Silicon in the Field of Optics. A review. *J. Mater. Sci.* **2010**, *45*, 2823−2838.
(16) Algasinger, M.; Paye, J.; Werner, F.; Schmidt, J.; Brandt, M. S.; Stutzmann, M.; Koynov, S. Improved Black Silicon for Photovoltaic Applications. *Adv. Energy Mater.* **2013**, *3*, 1068−1074.
(17) Jeong, S.; McGehee, M. D.; Cui, Y. All-Back-Contact Utra-Thin Silicon Nanocone Solar Cells with 13.7% Power Conversion Efficiency. *Nat. Commun.* **2013**, *4*, 2950.
(18) Lu, Y. R.; Lal, A. High-Efficiency Ordered Silicon Nano-Conical-Frustum Array Solar Cells by Self-Powered Parallel Electron Lithography. *Nano Lett.* **2010**, *10*, 4651−4656.
(19) Sharma, M.; Pudasaini, P. R.; Ruiz-Zepeda, F.; Elam, D.; Ayon, A. A. Ultrathin, Flexible Organic−Inorganic Hybrid Solar Cells Based


DOI: 10.1021/acsami.5b00677
*ACS Appl. Mater. Interfaces* 2015, 7, 10228−10237

on Silicon Nanowires and PEDOT:PSS. *ACS Appl. Mater. Interfaces* **2014**, *6*, 4356−4363.
(20) Li, X. P.; Xiao, Y. J.; Bang, J. H.; Lausch, D.; Meyer, S.; Miclea, P. T.; Jung, J. Y.; Schweizer, S. L.; Lee, J. H.; Wehrspohn, R. B. Upgraded Silicon Nanowires by Metal-Assisted Etching of Metallurgical Silicon: A New Route to Nanostructured Solar-Grade Silicon. *Adv. Mater.* **2013**, *25*, 3187−3191.
(21) Wu, S. L.; Wen, L.; Cheng, G. A.; Zheng, R. T.; Wu, X. L. Surface Morphology-Dependent Photoelectrochemical Properties of One-Dimensional Si Nanostructure Arrays Prepared by Chemical Etching. *ACS Appl. Mater. Interfaces* **2013**, *5*, 4769−4776.
(22) Kumar, D.; Srivastava, S. K.; Singh, P. K.; Husain, M.; Kumar, V. Fabrication of Silicon Nanowire Arrays Based Solar Cell with Improved Performance. *Sol. Energy Mater. Sol. C* **2011**, *95*, 215−218.
(23) Lin, X. X.; Hua, X.; Huang, Z. G.; Shen, W. Z. Realization of High Performance Silicon Nanowire Based Solar Cells with Large Size. *Nanotechnology* **2013**, *24*, 235402.
(24) Liu, Y. P.; Lai, T.; Li, H. L.; Wang, Y.; Mei, Z. X.; Liang, H. L.; Li, Z. L.; Zhang, F. M.; Wang, W. J.; Kuznetsov, A. Y.; Du, X. L. Nanostructure Formation and Passivation of Large-Area Black Silicon for Solar Cell Applications. *Small* **2012**, *8*, 1392−1397.
(25) He, L. N.; Lai, D.; Wang, H.; Jiang, C. Y. Rusli High-Efficiency Si/Polymer Hybrid Solar Cells Based on Synergistic Surface Texturing of Si Nanowires on Pyramids. *Small* **2012**, *8*, 1664−1668.
(26) Liu, X.; Coxon, P. R.; Peters, M.; Hoex, B.; Cole, J. M.; Fray, D. J. Black Silicon: Fabrication Methods, Properties and Solar Energy Applications. *Energy Environ.. Sci.* **2014**, *7*, 3223−3263.
(27) Cheng, Y. T.; Ho, J. J.; Tsai, S. Y.; Ye, Z. Z.; Lee, W.; Hwang, D. S.; Chang, S. H.; Chang, C. C.; Wang, K. L. Efficiency Improved by Acid Texturization for Multi-Crystalline Silicon Solar Cells. *Sol. Energy* **2011**, *85*, 87−94.
(28) Jang, H. S.; Choi, H. J.; Oh, B. Y.; Kim, J. H. Combinational Approach of Electrochemical Etching and Metal-Assisted Chemical Etching for p-Type Silicon Wire Formation. *Electrochem. Solid State* **2011**, *14*, D5−D9.
(29) Dussart, R.; Tillocher, T.; Lefaucheux, P.; Boufnichel, M. Plasma Cryogenic Etching of Silicon: from the Early Days to Today's Advanced Technologies. *J. Phys. D: Appl. Phys.* **2014**, *47*, 123001.
(30) Nguyen, K. N.; Basset, P.; Marty, F.; Leprince-Wang, Y.; Bourouina, T. On the Optical and Morphological Properties of Microstructured Black Silicon Obtained by Cryogenic-Enhanced Plasma Reactive Ion Etching. *J. Appl. Phys.* **2013**, *113*, 194903.
(31) Liu, K.; Qu, S. C.; Zhang, X. H.; Tan, F. R.; Bi, Y.; Lu, S. D.; Wang, Z. G. Sulfur-Doped Black Silicon formed by Metal-Assist Chemical Etching and Ion Implanting. *Appl. Phys. A: Mater. Sci. Process.* **2014**, *114*, 765−768.
(32) Umezu, I.; Warrender, J. M.; Charnvanichborikarn, S.; Kohno, A.; Williams, J. S.; Tabbal, M.; Papazoglou, D. G.; Zhang, X. C.; Aziz, M. J. Emergence of very Broad Infrared Absorption Band by Hyperdoping of Silicon with Chalcogens. *J. Appl. Phys.* **2013**, *113*, 213501.
(33) Chen, C. Y.; Li, W. J.; Chen, H. H. Tailoring Broadband Antireflection on a Silicon Surface through Two-Step Silver-Assisted Chemical Etching. *ChemPhysChem* **2012**, *13*, 1415−1420.
(34) Kumar, D.; Srivastava, S. K.; Singh, P. K.; Sood, K. N.; Singh, V. N.; Dilawar, N.; Husain, M. Room Temperature Growth of Wafer-Scale Silicon Nanowire Arrays and Their Raman Characteristics. *J. Nanopart. Res.* **2010**, *12*, 2267−2276.
(35) Matsui, Y.; Adachi, S. Optical Properties of "Black Silicon" Formed by Catalytic Etching of Au/Si(100) Wafers. *J. Appl. Phys.* **2013**, *113*, 173502.
(36) Srivastava, S. K.; Kumar, D.; Vandana Sharma, M.; Kumar, R.; Singh, P. K. Silver Catalyzed Nano-Texturing of Silicon Surfaces for Solar Cell Applications. *Sol. Energy Mater. Sol. C* **2012**, *100*, 33−38.
(37) Cho, S. K.; Fan, F. R. F.; Bard, A. J. Electrodeposition of Crystalline and Photoactive Silicon Directly from Silicon Dioxide Nanoparticles in Molten $CaCl_2$. *Angew. Chem., Int. Ed.* **2012**, *51*, 12740−12744.
(38) Juzeliunas, E.; Cox, A.; Fray, D. J. Electro-Deoxidation of Thin Silica Layer in Molten Salt-Globular Structures with Effective Light Absorbance. *Electrochim. Acta* **2012**, *68*, 123−127.
(39) Koynov, S.; Brandt, M. S.; Stutzmann, M. Black Thin Film Silicon. *J. Appl. Phys.* **2011**, *110*, 043537.
(40) Huang, Z. P.; Geyer, N.; Werner, P.; de Boor, J.; Gosele, U. Metal-Assisted Chemical Etching of Silicon: A Review. *Adv. Mater.* **2011**, *23*, 285−308.
(41) Oh, J.; Yuan, H. C.; Branz, H. M. An 18.237.22-Efficient Black-Silicon Solar Cell Achieved through Control of Carrier Recombination in Nanostructures. *Nat. Nanotechnol* **2012**, *7*, 743−748.
(42) Repo, P.; Benick, J.; Vähänissi, V.; Schön, J.; von Gastrow, G.; Steinhauser, B.; Schubert, M. C.; Hermle, M.; Savin, H. N-type Black Silicon Solar Cells. *Energy Proc.* **2013**, *38*, 866−871.
(43) Zhong, S. H.; Liu, B. W.; Xia, Y.; Liu, J. H.; Liu, J.; Shen, Z. A.; Xu, Z.; Li, C. B. Influence of the Texturing Structure on the Properties of Black Silicon Solar Cell. *Sol. Energy Mater. Sol. C* **2013**, *108*, 200−204.
(44) Zhong, S.; Huang, Z.; Lin, X.; Zeng, Y.; Ma, Y.; Shen, W. High-Efficiency Nanostructured Silicon Solar Cells on a Large Scale Realized Through the Suppression of Recombination Channels. *Adv. Mater.* **2014**, *27*, 555−561.
(45) Hoex, B.; Gielis, J. J. H.; de Sanden, M. C. M. V.; Kessels, W. M. M. On the C−Si Surface Passivation Mechanism by the Negative-Charge-Dielectric $Al_2O_3$. *J. Appl. Phys.* **2008**, *104*, 113703.
(46) Liu, W. F.; Bian, J. M.; Zhao, Z. C.; Luo, Y. L.; Yuan, Z.; Zhang, B. Y.; Liu, A. M. Low Temperature Surface Passivation of Black Silicon Solar Cells by High-Pressure $O_2$ Thermal Oxidation. *ECS Solid State Lett.* **2013**, *2*, Q17−Q20.
(47) Liu, S. Y.; Niu, X. W.; Shan, W.; Lu, W.; Zheng, J. Y.; Li, Y. F.; Duan, H. B.; Quan, W. J.; Han, W. Z.; Wronski, C. R.; Yang, D. R. Improvement of Conversion Efficiency of Multicrystalline Silicon Solar Cells by Incorporating Reactive Ion Etching Texturing. *Sol. Energy Mater. Sol. C* **2014**, *127*, 21−26.
(48) Yue, Z. H.; Shen, H. L.; Jiang, Y.; Chen, W. L.; Tang, Q. T.; Jin, J. L.; Pu, T.; Luo, J. W.; Kong, F. J.; Rui, C. B.; Cai, J. B. Large-Scale Black Multi-Crystalline Silicon Solar Cell with Conversion Efficiency over 18%. *Appl. Phys. A: Mater. Sci. Process.* **2014**, *116*, 683−688.
(49) Huang, Z.; Zhong, S.; Hua, X.; Lin, X.; Kong, X.; Dai, N.; Shen, W. An Effective Way to Simultaneous Realization of Excellent Optical and Electrical Performance in Large-Scale Si Nano/Microstructures. *Prog. Photovolt., Res. Appl.* **2014**, DOI: 10.1002/pip.2506.
(50) Ye, X. Y.; Zou, S.; Chen, K. X.; Li, J. J.; Huang, J.; Cao, F.; Wang, X. S.; Zhang, L. J.; Wang, X. F.; Shen, M. R.; Su, X. D. 18.45%-Efficient Multi-Crystalline Silicon Solar Cells with Novel Nanoscale Pseudo-Pyramid Texture. *Adv. Funct. Mater.* **2014**, *24*, 6708−6716.
(51) Dingemans, G.; Kessels, E. Status and Prospects of $Al_2O_3$-Based Surface Passivation Schemes for Silicon Solar Cells. *J. Vac. Sci. Technol. A* **2012**, *30*, 040802.
(52) Wang, W. C.; Lin, C. W.; Chen, H. J.; Chang, C. W.; Huang, J. J.; Yang, M. J.; Tjahjono, B.; Huang, J. J.; Hsu, W. C.; Chen, M. J. Surface Passivation of Efficient Nanotextured Black Silicon Solar Cells Using Thermal Atomic Layer Deposition. *ACS Appl. Mater. Interfaces* **2013**, *5*, 9752−9759.
(53) Wang, W.-C.; Lin, C.-W.; Ko, C.-T.; Yang, J.; Tjahjono, B.; Hsu, C.; Chen, M.-J. Efficiency Enhancement and Anti-Corrosion Protection on Silicon Solar Cells by Atomic-Layer-Deposited $Al_2O_3$ Conformal Shell Layer on Antireflective ZnO Nanorod Array. *ECS J. Solid State Sci. Technol.* **2014**, *3*, Q221−Q226.
(54) Fang, H.; Wu, Y.; Zhao, J. H.; Zhu, J. Silver Catalysis in the Fabrication of Silicon Nanowire Arrays. *Nanotechnology* **2006**, *17*, 3768−3774.
(55) Wu, M. K.; Shih, Y. T.; Chen, M. J.; Yang, J. R.; Shiojiri, M. Z ZnO Quantum Dots Embedded in a $SiO_2$ Nanoparticle Layer Grown by Atomic Layer Deposition. *Phys. Status Solidi R* **2009**, *3*, 88−90.
(56) Henkel, C.; Abermann, S.; Bethge, O.; Bertagnolli, E. Atomic Layer-Deposited Platinum in High-K/Metal Gate Stacks. *Semicond. Sci. Technol.* **2009**, *24*, 125013.


DOI: 10.1021/acsami.5b00677
*ACS Appl. Mater. Interfaces* 2015, 7, 10228−10237

(57) Choi, B. J.; Jeong, D. S.; Kim, S. K.; Rohde, C.; Choi, S.; Oh, J. H.; Kim, H. J.; Hwang, C. S.; Szot, K.; Waser, R.; Reichenberg, B.; Tiedke, S. Resistive Switching Mechanism of $TiO_2$ Thin Films Grown by Atomic-Layer Deposition. *J. Appl. Phys.* **2005**, *98*, 033715.
(58) Kim, S. K.; Choi, G. J.; Lee, S. Y.; Seo, M.; Lee, S. W.; Han, J. H.; Ahn, H. S.; Han, S.; Hwang, C. S. Al-Doped $TiO_2$ Films with Ultralow Leakage Currents for next Generation DRAM Capacitors. *Adv. Mater.* **2008**, *20*, 1429−1439.
(59) Terman, L. M. An Investigation of Surface States at a Silicon Silicon Oxide Interface Employing Metal Oxide Silicon Diodes. *Solid State Electron.* **1962**, *5*, 285−299.
(60) Cartier, E.; Stathis, J. H.; Buchanan, D. A. Passivation and Depassivation of Silicon Dangling Bonds at the $Si/SiO_2$ Interface by Atomic-Hydrogen. *Appl. Phys. Lett.* **1993**, *63*, 1510−1512.
(61) Henson, W. K.; Ahmed, K. Z.; Vogel, E. M.; Hauser, J. R.; Wortman, J. J.; Venables, R. D.; Xu, M.; Venables, D. Estimating Oxide Thickness of Tunnel Oxides down to 1.4 nm Using Conventional Capacitance-Voltage Measurements on MOS capacitors. *IEEE Electron Device Lett.* **1999**, *20*, 179−181.
(62) Weber, J. R.; Janotti, A.; Van de Walle, C. G. Native Defects in $Al_2O_3$ and Their Impact on III−V/$Al_2O_3$ Metal-Oxide-Semiconductor-Based Devices. *J. Appl. Phys.* **2011**, *109*, 033715.
(63) Shin, B.; Weber, J. R.; Long, R. D.; Hurley, P. K.; Van de Walle, C. G.; McIntyre, P. C. Origin and Passivation of Fixed Charge in Atomic Layer Deposited Aluminum Oxide Gate Insulators on Chemically Treated InGaAs Substrates. *Appl. Phys. Lett.* **2010**, *96*, 152908.
(64) Ahn, Y.; Choudhury, S. H.; Lee, D.; Sadaf, S. M.; Siddik, M.; Jo, M.; Park, S.; Kim, Y. D.; Kim, D. H.; Hwang, H. Estimation of Interfacial Fixed Charge at $Al_2O_3/SiO_2$ Using Slant-Etched Wafer for Solar Cell Application. *Jpn. J. Appl. Phys.* **2011**, *50*, 071503.
(65) Lei, D.; Yu, X. G.; Song, L. H.; Gu, X.; Li, G. H.; Yang, D. R. Modulation of Atomic-Layer-Deposited $Al_2O_3$ Film Passivation of Silicon Surface by Rapid Thermal Processing. *Appl. Phys. Lett.* **2011**, *99*, 052103.
(66) Johnson, R. S.; Lucovsky, G.; Baumvol, I. Physical and Electrical Properties of Noncrystalline $Al_2O_3$ Prepared by Remote Plasma Enhanced Chemical Vapor Deposition. *J. Vac. Sci. Technol. A* **2001**, *19*, 1353−1360.
(67) Doeswijk, L. M.; de Moor, H. H. C.; Blank, D. H. A.; Rogalla, H. Passivating $TiO_2$ Coatings for Silicon Solar Cells by Pulsed Laser Deposition. *Appl. Phys. A: Mater. Sci. Process.* **1999**, *69*, S409−S411.
(68) Richards, B. S. Comparison of $TiO_2$ and other Dielectric Coatings for Buried-Contact Solar Cells: a review. *Prog. Photovoltaics* **2004**, *12*, 253−281.
(69) Bowden, S.; Yelundur, V.; Rohatgi, A. Implied-$V_{oc}$ and Suns-$V_{oc}$ Measurements in Multicrystalline Solar Cells, Photovoltaic Specialists Conference. *Conference Record of the Twenty-Ninth IEEE*, May 19−24, 2002; IEEE: Piscataway, NJ, 2002; pp 371−374.


DOI: 10.1021/acsami.5b00677
*ACS Appl. Mater. Interfaces* 2015, 7, 10228−10237